INVESTIGATION OF THE FERMI SURFACE AND OF CARRIER VELOCITIES IN INDIUM BY THE CYCLOTRON RESONANCE METHOD

R. T. MINA and M. S. KHAĬKIN

Institute for Physics Problems, Academy of Sciences, U.S.S.R.; Physics Institute, State Atomic Energy Commission

Submitted to JETP editor February 11, 1966

J. Exptl. Theoret. Phys. (U.S.S.R.) 51, 62–86 (July, 1966)

The results are presented of systematic investigations of the cyclotron resonance in indium single crystals. The measurements were carried out at a frequency of 18.7 Gc and sample temperature of 1.5°K. The anisotropy of the effective hole and electron masses was investigated in the crystallographic planes $(0\bar{1}0)$, $(1\bar{1}0)$, $(1\bar{1}1)$, $(0\bar{1}1)$, and (001). An analysis of the results obtained made it possible to find the carrier velocities on the Fermi surface. For example, the hole velocity was determined along a surface "rib" lying in the (001) Brillouin plane, and was found to be 0.73×10^8 cm/sec. It was established that the effective mass anisotropy (variation from 0.11 to 2.2 m_e, i.e., by a factor of 20) and the carrier velocity anisotropy (variation from 0.73×10^8 to 1.10×10^8 cm/sec, i.e., by a factor of 1.4) were in good agreement with the almost-free electron model (1-OPW), in which the carrier mass m_c was taken to be 1.6 m_e. The dimensions of the hole Fermi surface along the directions [100] and [001] (0.91 and 0.78 h/a, respectively) were determined using the cyclotron resonance cutoff effect in a thin sample. A number of experimental observations were obtained which were not consistent with the 1-OPW model. To explain them, calculations were made of some features of the Fermi surface model in the 2-OPW approximation, which made it possible to determine the effective potentials of the indium lattice: $|V_{111}| = 0.07 \pm 0.015$, $|V_{002}| = 0.055 \pm 0.01$, $|V_{200}| < 0.015$ [in $(h/a)^2/2m_c = 0.329$ Ry units].

ACCORDING to the model of almost-free electrons, the Fermi surface of indium consists of two parts: a hole surface in the second zone and an electron surface in the third zone, the volumes of these parts differing by about one order of magnitude. The systematic experimental investigation of the Fermi surface of indium began only relatively recently. The majority of the investigations,[1-6] carried out by various methods, dealt with the shape of the Fermi surface. The ultrasonic investigations of Rayne[1] have basically confirmed the almost-free electron model of indium, showing that the dimensions of one part of the surface are approximately three times as large as those of the other part. Fuller data on the electron Fermi surface of indium have been obtained by investigating the de Haas–van Alphen effect.[2] From this study, Brandt and Rayne have deduced that the electron surface consists of tubes which become narrower at their ends, and whose axes are directed along [110] and $[1\bar{1}0]$. Also, oscillations have been observed in the case of tubes elongated along the [011] and equivalent axes; the former are called the β tubes, and the latter the α tubes. The exact dimensions of the Fermi surface have been found by Gantmakher and Krylov[3] by investigating the radio-frequency size effect. They have been able to show that the β tubes are joined end to end and form a surface topologically equivalent to a torus, but they have not obtained any information on the α tubes. Several investigations of the galvanomagnetic properties of indium, of which Gaĭdukov's recent measurements[4] were the most accurate and complete, have established that indium has no open trajectories.

The first observations of the cyclotron resonance (c.r.) by Castle, Chandrasekhar, and Rayne[5] have shown that there are two groups of effective masses in indium, differing by a factor of about three. The systematic investigation of the c.r. was begun by the present authors,[6] who have established that the strongest resonances occur for the hole orbits of the Fermi surface in the second zone, when the direction of the magnetic field is close to the directions of the axes [001] and [100], as well as for the electron orbits of the Fermi surface in the third zone. This investigation[6] also included experiments on the c.r. cut-

off in a thin sample, from which the extremal dimensions of the hole surface along the [001] direction have been obtained. The results of these measurements are in good agreement with the data on the size effect.[3] Further investigations, reported in the present paper, have established new c.r. in the $(0\bar{1}0)$, $(1\bar{1}1)$, and (001) planes, which were investigated in a preliminary way in [6]; the anisotropy of these resonances was found, the crystallographic planes $(1\bar{1}0)$ and $(0\bar{1}1)$ were investigated, and the main dimensions of the hole surface were determined from the c.r. cutoff.

The determination of the carrier velocities and their anisotropy was regarded as no less important than the investigation of the shape of the Fermi surface. There are several experimental methods for determining the carrier velocity.

1. Measurements of the electronic contribution to the specific heat[7] make it possible to determine the carrier velocity averaged out over the whole Fermi surface.

2. The value of the effective carrier mass for a narrow strip of the Fermi surface can be used to find the average velocity along such a strip. The effective mass is found from the temperature dependence of the amplitude of quantum oscillations[2] or, more accurately, by the c.r. method. As shown in the present paper, the distribution of velocities on the Fermi surface can be deduced from the anisotropy of the average velocity for various directions of the magnetic field.

3. In those cases when the c.r. can be detected at an elliptical limiting point, the carrier velocity at that point can be determined from the value of the effective mass and that of the Fermi surface curvature. The velocity of holes along the [111] direction was found in this way.[8]

4. The velocity of carriers at an elliptical limiting point of the Fermi surface can be also determined by measuring the c.r. shift due to the Doppler effect when a magnetic field is directed obliquely to the surface of the sample. A knowledge of the electromagnetic field distribution in an indium skin layer (investigated in [8]) makes it possible to determine the velocity of electrons at several points of the electron Fermi surface. Such experiments will be described in a separate communication.

5. Very recently, a new method of measuring the carrier velocity has been discovered. In a film structure, one of whose components is a thin polycrystalline layer of indium, tunnel current oscillations have been observed.[9] This effect makes it possible to determine the carrier velocity in indium, which is found to be $v_F = 1.23 \times 10^8$ cm/sec.

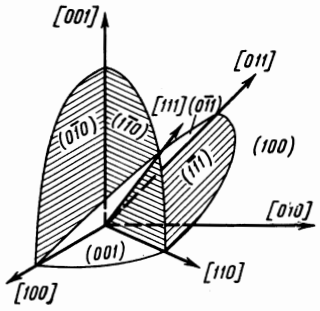

FIG. 1. Orientations of the plane surfaces of the samples (cf. Table I).

On the whole, the results of the present investigation (like those reported in [1-9]) are in good agreement with the model of almost-free electrons, developed in the approximation of one orthogonalized plane wave (1-OPW), if the effective lattice potential is assumed to be negligibly small.[10] Slight differences between the experiment data and and the 1-OPW model, found in the present investigation, are satisfactorily accounted for by the 2-OPW model, for which a certain effective lattice potential is assumed.

EXPERIMENT

The measurements were carried out by the frequency modulation method[11] at 18.7 Gc; the logarithmic derivative of the reactive component of the surface impedance of the metal was determined. The samples were indium single crystals containing less than 10^{-3}% impurities. The samples were grown from the melt in a polished demountable quartz mold and were in the form of disks, 18 mm in diameter and 1 or 0.24 mm thick; their properties are given in Table I and Fig. 1. To prepare thin samples, we placed, in a disk-shaped quartz mold, a quartz disk of the same diameter as the mold but thinner, so that the sum of the thicknesses of the quartz disk and the sample was 1 mm. After dismantling the mold, the grown single crystal was placed in a strip resonator, similar to that shown in Fig. 1a in [12]. A half-

Table I

Sample	Thickness, mm	Angle between indicated axis and its projection on sample surface				Orientation of plane surface of sample* (cf. Fig. 1)
		[100]	[110]	[011]	[001]	
I	1	2°20′			45′	(0$\bar{1}$0)
II	1		2°15′		3°	(1$\bar{1}$0)
III	0.24		1°40′		2°50′	(1$\bar{1}$0)
IV	1		5°50′		20′	(1$\bar{1}$0)
V	1		30′	50′		(1$\bar{1}$1)
VI	1	1°10′		20′		(0$\bar{1}$1)
VII	0.24	2°50′	0′			(001)

*Within error governed by the orientations listed in the table.

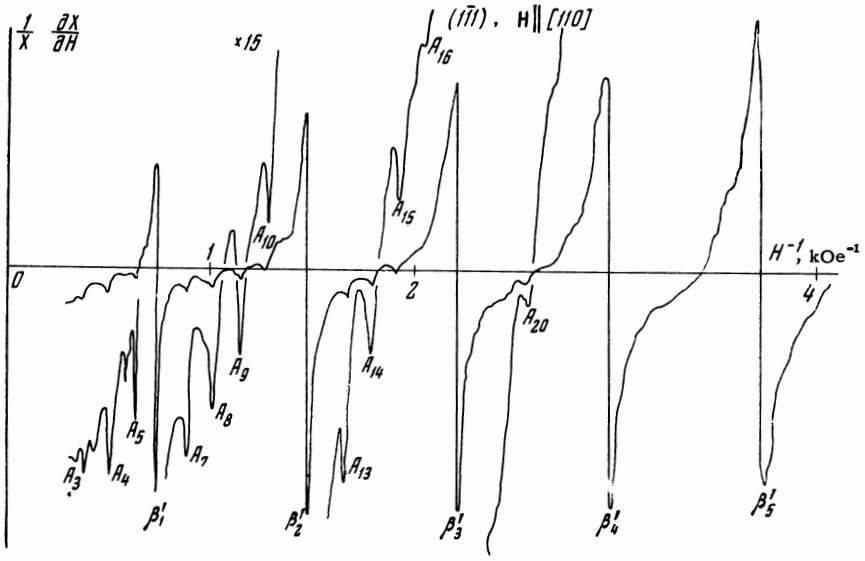

FIG. 2. Recordings of the logarithmic derivative of the reactive component of the surface impedance of indium as a function of the reciprocal of the magnetic field. The sample and field orientation are given at the top of the figure. Two series of c.r. are denoted by A and β'; the subscripts indicate the order of the c.r. In the intervals between neighboring β' c.r., the amplification of the system was increased by a factor of 15 before the next recording.

wave resonance strip had the dimensions 6.5 × 3 × 1 mm. Thus, high-frequency currents were flowing only along the central part of the sample, representing about a tenth of its surface area. As shown in Fig. 1a in [12], the single crystal was not fixed to the resonator but was freely supported by a horizontal quartz disk so that repeated cooling of the sample did not damage it.

The average thickness of a thin sample, determined on completion of the experiments, was found to be equal to the difference between the heights of the substrate surface and several points on the sample's surface. A double microscope of the MIS-11 type was used as an indicator of the position of the surface to within 0.5 μ, without making contact with the surface; the vertical motion of the microscope was measured with an optical level to within 0.2 μ. The average thickness of both thin samples InIII and InVII was found to be the same and equal to 0.240 ± 0.002 mm.

A magnetic field **H** was applied parallel to the flat surface of a sample. The field could be rotated through any angle in the plane of the surface of the sample and could be inclined to the surface by up to ~1°. The rotation was measured to within ±15′ by means of a circular scale fixed to an electromagnet, and the inclination was measured with a quadrant optical lever to within ±15″. An inclination of the electromagnet up to 10′ could be determined by means of an autocollimator of the AKT-250 type to within ±2″.

At helium temperatures, the sample and its support could be rotated in the resonator, about a vertical axis, with respect to the resonator strip. This altered the polarization of the high-frequency currents in the sample with respect to the crystallographic axes. The position of a sample with respect to the poles of the electromagnet was determined, to within ±5′, from the disappearance of the modulation signal found separately for two mutually perpendicular coils fixed to the sample support in such a way that the axis of one coil was perpendicular, and the other parallel, to the surface of the sample.

The sample temperature was identical with the temperature of the helium bath and, as the helium level in the cryostat fell during experiments lasting 4–5 hours, it decreased from 1.8 to 1.5° K. The lowering of the temperature from 4.2 to 1.5° K increased the c.r. amplitude by a factor of 8–10.

The direct result of the experiments was the recording of the dependence of the logarithmic derivative of the reactive component of the surface impedance of indium on the reciprocal of the magnetic field intensity, which was measured by means of a Hall probe and calibrated with a nuclear magnetometer. A typical recording of the c.r. spectra is given in Fig. 2. It shows clearly the resonances with two periods differing by a factor of almost six. The period ΔH^{-1} corresponds to an effective mass μ, calculated from the formula[6,8]

$$\mu = m^*/m_e = H_{EPR}/\Delta H^{-1} = e/m_e c\omega \Delta H^{-1}. \quad (1)$$

The anisotropy of the effective masses, found by means of this formula for all the principal crystallographic planes, is shown in Figs. 3–7, as well as in Figs. 11 and 12. The good agreement between the results of the measurements carried out on different samples is illustrated on Fig. 7, which gives the effective masses obtained in experiments on two samples. Figure 4 also gives the values of the effective masses measured for two samples which differed considerably in their crystallographic orientations, as given in Table I. The in-

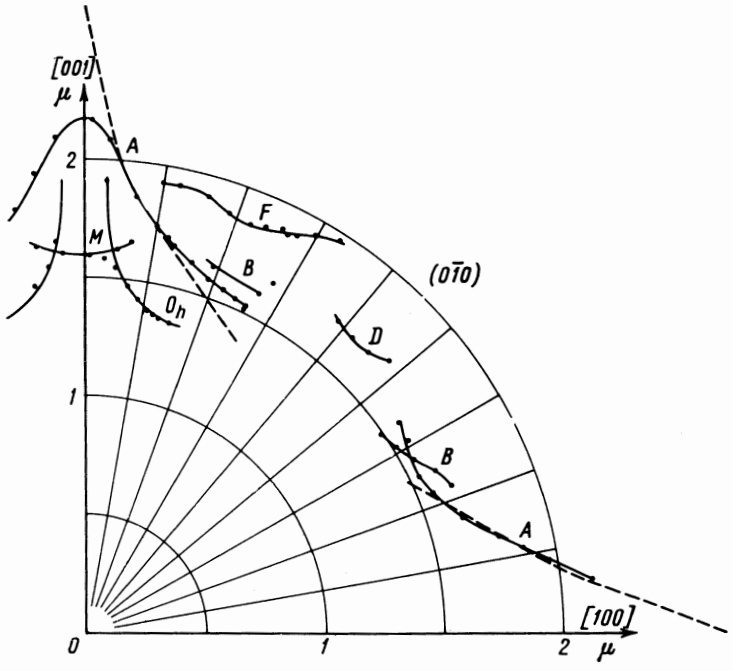

FIG. 3. Anisotropy of the effective mass of holes in indium in the (0$\bar{1}$0) plane. Sample InI. The dashed curve represents the effective mass A, calculated using the 1-OPW model and multiplied by the coefficient k given in Table IV (see below).

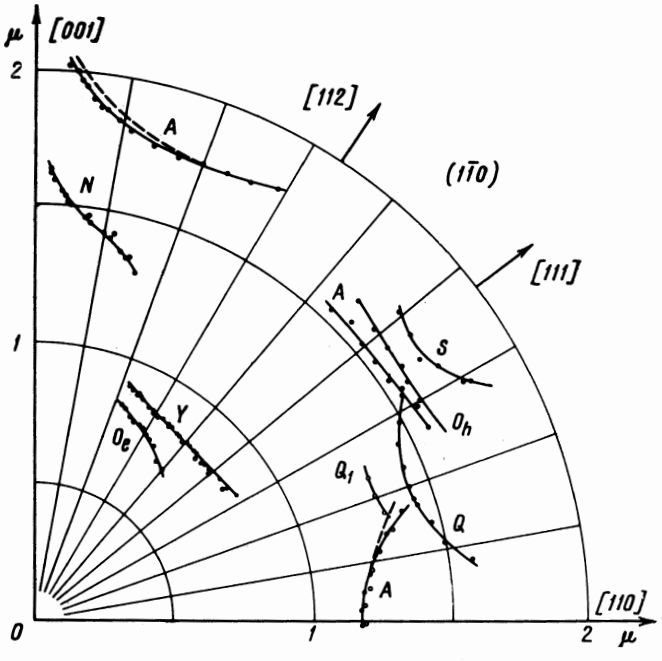

FIG. 4. Anisotropy of the effective masses of holes and electrons at a limiting point O_e on the electron Fermi surface of indium in the (1$\bar{1}$0) plane. The points refer to the masses measured in samples InII (●) and InIV (○). The dashed curve has the same meaning as in Fig. 3.

fluence of a small change in the sample orientation on the effective mass anisotropy helped in the interpretation of the experimental results, as will be shown below.

It has been shown earlier[6,8] that the carriers whose effective masses are larger than 0.8–0.9 refer to the hole Fermi surface in the second zone and the carriers of lower masses refer to the electron Fermi surface in the third zone. In accordance with this distinction, we shall consider separately the respective results.

HOLE FERMI SURFACE OF INDIUM IN THE SECOND ZONE

Measurements of the Effective Hole Masses

Figures 3–7 show the anisotropy of the effective carrier masses for the second-zone Fermi surface (with the exception of masses denoted by O_e). Some of the data on the strongest lines in the (0$\bar{1}$0) and (001) planes have already been reported in [6]. The results given in Fig. 3 were obtained for a sample with a more precise crystallographic

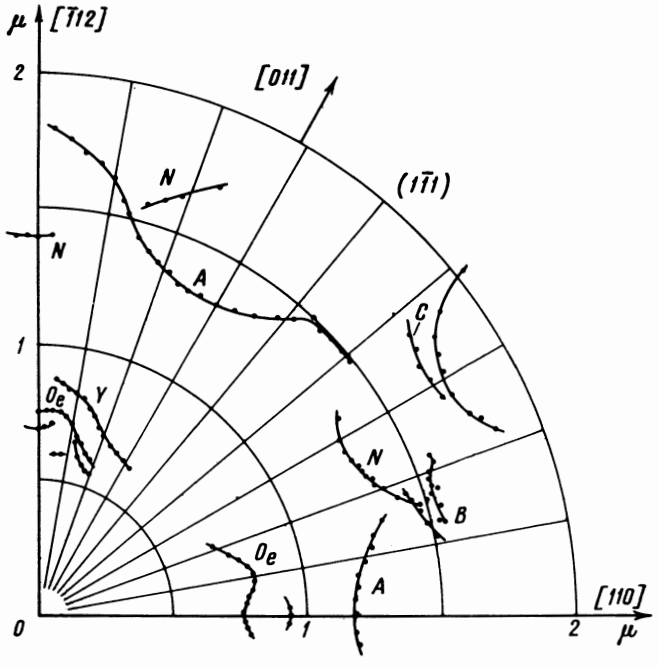

FIG. 5. Anisotropy of the effective masses of holes and electrons at a limiting point O_e on the electron Fermi surface in indium in the (1$\bar{1}$1) plane. Sample InV.

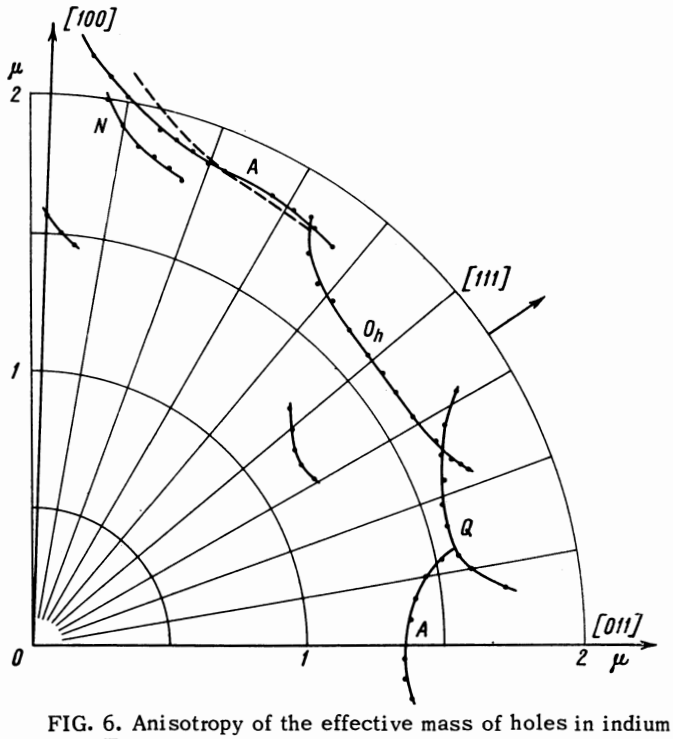

FIG. 6. Anisotropy of the effective mass of holes in indium in the (0$\bar{1}$1) plane. Sample InVI. The dashed curve has the same meaning as in Fig. 3.

orientation of its surface and, therefore, some effective masses (for example, for H‖[001]) were found more accurately.

As shown before,[6] the shapes of the hole Fermi surfaces of indium (see below in Fig. 10) and aluminum[10] are very similar. The only difference is a slight compression of the Fermi surface of indium along the tetragonal [001] axis direction, by about ~16% according to the 1-OPW model (the model was developed for a tetragonal face-centered crystal lattice with the constants a = 4.58 Å, c/a = 1.078. This made it possible to identify the c.r. using the calculations of the effective hole mass anisotropy of aluminum, carried out by Naberezhnyĭ and Tolstoluzhskiĭ.[13] The effective masses of carriers in indium are denoted in Figs. 3–7 by the same symbols as were used in Fig. 2 in [13] to denote the calculated effective masses in aluminum, which had similar anisotropy. We used, of course, other characteristic properties to assign the c.r. to given orbits on the hole surface; among these properties were, for example, the dependence of the c.r. amplitude on the polarization of the high-frequency currents **J** and on the inclination of the magnetic field to the surface of the sample, etc., which are discussed in detail later.

Central Hole Orbits

In all the investigated planes we observed an intense c.r. A for the central cross section of the Fermi surface (see Fig. 10 below), exhibiting a very characteristic effective mass anisotropy near the crystallographic axes [100] and [001] (Figs. 3 and 7). The amplitude of this c.r. was maximal for **H** ⊥ **J** and vanished for **H** ∥ **J**. As a rule, it depended weakly on the inclination of the magnetic field to the surface of the sample. When the magnetic field was rotated, the orbit A crossed singularities (vertices) W and W′ of the hole surface (Figs. 7 and 10) where the intensity of the c.r. A decreased so suddenly that it disappeared in the noise level, with the exception of the **H**∥[001] case. In the latter case, the c.r. amplitude was much weaker and very sensitive to the inclination of the magnetic field to the surface of the sample (Fig. 5 in [6]). This characteristic influence of the singularities W and W′ of the hole surface on the c.r. A amplitude was well confirmed by a comparison of the angular intervals given in Table II, which showed that the c.r. A was observed with the intervals predicted by the 1-OPW model (see Fig. 10 below).

Thus, in spite of the fact that the hole Fermi surface of indium was closed,[4] the c.r. A along the central section did not remain continuous when the magnetic field was rotated in any crystallographic plane. Figures 3 and 5–7 show clearly that in some angular intervals, between the directions corresponding to the singularities W and W′, the effective mass A vanished. This was be-

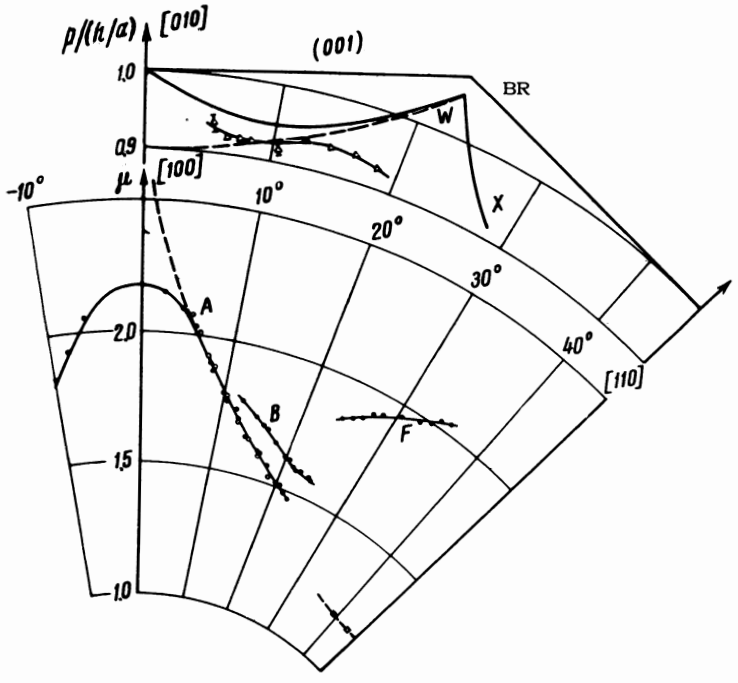

FIG. 7. Anisotropy of the effective mass of holes in indium in the (001) plane and the extremal dimensions of the central orbit A along a direction perpendicular to the magnetic field and to the normal at the surface of a sample. The points represent the following samples: ●– sample used in[6], ○ and △– InVII, □– InII, ■– InIV. The continuous thick lines are: BR – the boundaries of the Brillouin zone; X – a cross section of the hole surface of the 1-OPW model. The dashed curve has the same meaning as in Fig. 3.

cause[6] the hole orbits had fairly acute "angles" (Fig. 7 in [6]). When the "angle" of an orbit lay in the skin layer, the duration of the interaction of the electromagnetic field with a hole decreased so that the c.r. amplitude fell or disappeared completely in the noise background. Therefore, for example, the c.r. A was not observed for $\mathbf{H} \parallel [110]$ in the (001) plane, but it was seen clearly for the same direction of the magnetic field in the $(1\bar{1}1)$ plane (Fig. 4). This can be seen clearly by a comparison of Fig. 1 with Fig. 2 in [6]. Another example is the observation of the c.r. A for $\mathbf{H} \parallel [001]$ in the $(0\bar{1}0)$ plane but not in the $(1\bar{1}0)$ plane (Figs. 3 and 4).

The influence of the shape of the orbit on the c.r. amplitude did not make it possible to investigate the effective mass anisotropy in some planes using only one sample. However, this difficulty could be overcome by investigating a series of samples selected so that their surface planes included the necessary crystallographic directions and the investigated c.r. amplitude had the optimal value. This approach was used, for example, to determine the anisotropy of the effective mass A in the (001) plane near the [110] axis (Fig. 7), using samples InII and InIV, which differed slightly in their orientations (Table I). We then found that the rotation of the magnetic field by 6° from the [110] axis in the (001) plane, which was orthogonal to the plane in Fig. 4, increased the effective mass A by ~2%, in agreement with the 1-OPW model calculations. Such experiments helped in the interpretation of the experimental results.

Noncentral hole orbits

The polar diagrams of Figs. 3–7 include several plots of the effective masses for the c.r. along noncentral cross sections of the hole Fermi surface. As mentioned earlier, they were identified by a comparison with the calculations[13] for aluminum. In this procedure, the angular intervals in which the noncentral c.r. was observed had to be close to the calculated values (Table II) and the ratios of the various effective masses had to be approximately the same as the ratios of the corresponding calculated values. We were unable to identify by this procedure the c.r. Y, observed in the $(1\bar{1}0)$ (Fig. 3) and $(1\bar{1}1)$ (Fig. 5) planes; it was not clear to which orbit on the Fermi surface this c.r. belonged. It should be mentioned that the angular interval in which the c.r. Y was observed in both planes practically coincided with the interval of the existence of the y line in the size effect.[3]

The diagrams of Figs. 3, 4, and 6 include plots of the effective masses denoted by the symbol O_h, which refers to the c.r. at elliptical special points of the hole Fermi surface.[8] The corresponding orbits obviously lay on "caps" of the hole surface (cf. Fig. 10) for $\mathbf{H} \parallel [001]$ and $\mathbf{H} \parallel [111]$. In the latter case, the c.r. was strongest; c.r. of the order $n = 1-26$ were observed, corresponding to an effective mass $\mu = 1.605 \pm 0.005$, which was almost isotropic over a fairly wide range of angles in both planes $(1\bar{1}0)$ and $(0\bar{1}1)$ (Figs. 4 and 6). Thus, this part of the hole surface, which was furthest from

Table II

Cross sections	Type of c.r.	Plane	Calculation using 1–OPW model: Range of existence of orbit	Calculation using 1–OPW model: Interval, deg	Experiment: Интервал, град
Central	A	$(0\bar{1}0)$	$31° > \sphericalangle H, [100] > 0°$	31	34
	A	$(0\bar{1}0)$	$24° > \sphericalangle H, [001] > 0°$	24	26
	A	$(1\bar{1}0)$	$32° > \sphericalangle H, [001] > 0°$	32	29
	A	$(1\bar{1}0)$	$23° > \sphericalangle H, [110] \geqslant 0°$	23	17
	A	$(1\bar{1}1)$	$22° > \sphericalangle H, [110] \geqslant 0°$	22	16
	A	$(1\bar{1}1)$	$90° \geqslant \sphericalangle H, [110] > 43°$	47	44
	A	$(0\bar{1}1)$	$30° > \sphericalangle H, [100] > 0°$	30	35
	A	$(0\bar{1}1)$	$16° > \sphericalangle H, [011] \geqslant 0°$	16	15
	A	(001)	$28° > \sphericalangle H, [100] > 0°$	28	23
Noncentral	M	$(0\bar{1}0)$	$8° > \sphericalangle H, [001] \geqslant 0°$	8	7
	D	$(0\bar{1}0)$	$51° > \sphericalangle H, [001] > 39°$	12	10
	F	$(0\bar{1}0)$	$35° > \sphericalangle H, [001] > 15°$	20	23
	Q	$(1\bar{1}0)$	$32° > \sphericalangle H, [110] > 5°$	27	25
	N	$(1\bar{1}0)$	$20° > \sphericalangle H, [001] > 5°$	15	14
	Q	$(0\bar{1}1)$	$32° > \sphericalangle H, [011] > 5°$	27	24
	N	$(0\bar{1}1)$	$20° > \sphericalangle H, [100] > 5°$	15	10
	F	(001)	$35° > \sphericalangle H, [100] > 15°$	20	13

all the ribs, was distorted least and could be considered to be a part of a Fermi sphere.

The effective mass, corresponding to the c.r. at an elliptic limit point, is[14]

$$m^* = (v_F \sqrt{K})^{-1}. \quad (2)$$

For a Fermi sphere of radius p_c, the Gaussian curvature of the surface is $K = 1/p_c^2$ and the velocity is $v_F = v_c$, so that

$$\mu = m^* / m_e = (p_c / v_c) / m_e = m_c / m_e, \quad (3)$$

where m_c is the hole mass whose experimental value is $1.6m_e$. The hole velocity is $v_c = 1.09 \times 10^8$ cm/sec (the subscript "c" will be used always to denote values referring to the 1-OPW model, which is constructed using Fermi spheres[10]).

The difference between the free-electron mass and the mass of carriers in a metal has been found previously for lead,[15] aluminum,[13,16] and other metals; it is due to the existence of the electron–phonon interaction.

Principal dimensions of the hole surface

The c.r. cutoff is one of the most accurate methods of determining the dimensions of the Fermi surface. In [6] we reported a determination of the cutoff of the c.r. A in the central cross section of the hole surface, when the magnetic field direction was close to the [100] axis in the $(0\bar{1}0)$ plane (Figs. 8 and 9 in [6]). In the present investigation, these experiments were extended to thinner samples InIII and InVII (Table I).

A recording of the cutoff of the c.r. A in sample InVII is shown in Fig. 8. To determine exactly the cutoff field H_{co}, we were able to use the following characteristic properties of the c.r. A. As mentioned earlier, the effective mass A increased rapidly as the magnetic field direction approached the [100] axis (Fig. 7). Thus, in the angular interval $5° \leq \sphericalangle H, [100] \leq 8°$ (Fig. 8), the increase was

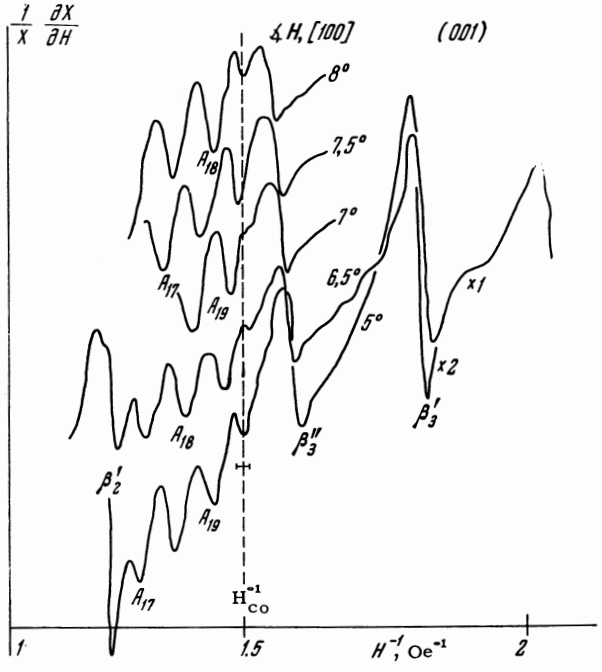

FIG. 8. Recording of the c.r. cutoff for the hole Fermi surface of indium. The orientation of the surface of a sample and the field are given (for each curve) in the figure. A is the c.r. on the hole surface, and β', β'' are the c.r. on the electron surface. The subscripts indicate the order of the resonance. The amplification of the circuit was doubled for each curve (going down). The dashed line shows the cutoff field H_{co}, and the accuracy of its measurement is indicated by a segment intersecting the dashed line.

Table III

Type of c.r.	Plane	Magnetic field direction	$p_{max}/(h/a)$ present study	$p_{max}/(h/a)$ ref. [3]	$p_{min}/(h/a)$ ref. [1]
A	(001)	$\sphericalangle$ **H**, [100] = 7°	0.915±0.015	0.93±0.02	0.88
A	(0$\bar{1}$0)	$\sphericalangle$ **H**, [001] = 20°	0.855±0.015 *	0.86±0.02	0.83
A	(1$\bar{1}$0)	**H** ∥ [110]	0,780±0.010	0.80±0.015	0.75
Q	(1$\bar{1}$0)	$\sphericalangle$ **H**, [110] = 20°	0.685±0.010	—	—

*Data from [6].

~5%, but the dimension of the orbit A did not change: according to the 1-OPW model, the maximum change in this angular range should be ~1%. Consequently, we were able to follow the various phases of the disappearance of the cutoff c.r. (for example, c.r. A_{19} in Fig. 8) in recordings of the c.r. spectra characterized by small angles of rotation of the field H. The accuracy of the determination of the cutoff field was higher for such a series of recordings and, in our case, amounted to ~2% (the probable error is shown by a segment in Fig. 8). This method for the exact determination of the cutoff field was similar to that used in [12], where the c.r. cutoff was shifted by a small change in the electromagnetic field frequency. From the value of H_{co} and the thickness D of a sample, we could calculate the external dimensions of the orbit in the momentum space using the formula:[12, 6]

$$p = eH_{co}D / 2c. \quad (4)$$

The upper part of Fig. 7 shows the anisotropy of the extremal dimensions of the orbit A calculated using formula (4). The dashed curve in Fig. 8 represents the central cross section of the hole surface (1-OPW model) for **H** ∥ [100] and the continuous curve X shows the projection of the ribs on this surface onto the (001) plane. The fact that, over the whole range of angles $\sphericalangle$ **H**, [100] = 5–20°, the measured values of the dimensions were less than the values given by the 1-OPW model, indicated that the ribs on the hole surface were rounded and the cusp near the point W was fairly smooth.

Table III lists all the dimensions determined by the c.r. cutoff method for indium. According to the 1-OPW model, the dimension p/(h/a), determined for $\sphericalangle$ **H**, [001] = 20°, should be larger by a factor of cos 20° than the dimension found for **H** ∥ [110]. We can easily show that the values (0.855 ± 0.01) cos 20° = 0.80 ± 0.01 and 0.78 ± 0.01 do indeed coincide, within the limits of the errors in the sample orientation.

As expected, in the tetragonal lattice of indium, the dimensions of the hole surface are different along the [001] and [100] axes: the former is 0.78(h/a), while the latter is 0.915(h/a) cos 7° = 0.91(h/a) (Table III). The ratio of these dimensions, which is 0.86 ± 0.02, is almost identical with the value $[2(h/c) - p_c]/[2(h/a) - p_c] = 0.84$, which follows from the 1-OPW model.

Table III gives the dimensions of the orbit corresponding to a noncentral c.r. Q. Information on the dimensions of the noncentral orbits is very important for the determination of their positions on the Fermi surface. It is then possible to calculate the value of the effective mass directly from the model without finding the extremum of this mass along the projection of p_H onto the direction of the magnetic field **H**. For this reason, the effective mass Q, is the only one of the masses corresponding to the noncentral orbits to be given in Table IV.

Table III includes, for comparison, the data obtained by the size effect method.[3] The results obtained by the two methods agree within the limits of the experimental error; however, Table III shows a small systematic difference between the results. The main cause of the difference was that, in the experiments of Gantmakher and Krylov[3] carried at 3 Mc, the depth of the skin layer was an order of magnitude greater than the depth for 18.7 Gc. Consequently, the range of fields in which the c.r. cutoff took place was less than the corresponding range (i.e., the line width) in the size effect. For the same reason (different depths of the skin layer), the numbers of electrons contributing to the two effects differed strongly. In the c.r. case, the number of these electrons was less and, consequently, the effect was weaker, which restricted the possibility of its observation. Thus, the c.r. cutoff method gave more accurate values of the cutoff field than the size effect but the former could be applied only over a narrow range of experimental conditions.

The experiments on the c.r. cutoff gave the following results. Using these results, we were able to compare such different characteristics of the investigated orbit as the effective mass and the external dimension; this made it possible to determine the average velocity of carriers in the

orbit.[6] In the case of the cutoff of the noncentral c.r., the measurements of the extremal orbit dimension made it possible to find the orbit position on the Fermi surface. Moreover, the c.r. spectrum in fields less than the cutoff field was simpler, which made it easier to interpret the spectrum.

The c.r. cutoff and the size effect[3] can be used only to determine the maximum dimension of the orbit, extremal in respect of p_H. Nonconvex Fermi surfaces, such as the hole surface of indium, have minimal dimensions of the orbits, extremal in respect of p_H, which can be measured by the ultrasonic absorption method[1] (Table III). The systematic difference between Rayne's results[1] and those reported here and in Gantmakher and Krylov's paper,[3] shows that, in spite of the smoothing of the ribs of the hole surface, the latter remains nonconvex.

Calculation of the effective masses and velocities of carriers

As shown in [15], the calculation of the effective mass

$$m^* = \frac{1}{2\pi} \oint dl/v_{F\perp} \qquad (5)$$

using the 1-OPW model reduces to the determination of the sum of the angular dimensions of the arcs of which the orbit is made up. Then, the velocity v_F over the whole Fermi surface is assumed to be the same and equal to

$$v_F = v_c = p_c / m_c, \qquad (6)$$

where m_c is the mass of a carrier moving at a velocity v_c on a Fermi sphere of radius p_c. On the ribs, which are located at intersections of the Fermi spheres and consequently lie in the Brillouin planes, the velocity $\hat{v}_c$ remains indeterminate. It can be calculated by the 2-OPW model. If $\mathbf{g}/h$ is the reciprocal lattice vector, perpendicular to a Brillouin plane, and

$$V_g = \int V(\mathbf{r})\, e^{i\mathbf{g}\mathbf{r}/h} d^3\mathbf{r}$$

is the Fourier component of the lattice potential, the relationship between the energy and momentum [according to formula (11.13) in [17]] is given by the expression

$$2m_c\varepsilon = g^2/4 + p_\perp^2 + p_\parallel^2 \pm [g^2 p_\parallel^2 + (2m_c V_g)^2]^{1/2}, \qquad (7)$$

where $p_\parallel$ and $p_\perp$ are the components of the momentum parallel and perpendicular to the vector $\mathbf{g}$, measured from the point of intersection of the vector $\mathbf{g}$ with the Brillouin plane. Using Eq. (7), we find the corresponding components of the carrier velocity $\mathbf{v}$:

$$v_\parallel = \partial\varepsilon/\partial p_\parallel = (1/m_c) p_\parallel \{1 \pm g^2 [g^2 p_\parallel^2 + (2m_c V_g)^2]^{-1/2}\},$$

$$v_\perp = \partial\varepsilon/\partial p_\perp = (1/m_c) p_\perp, \qquad (8)$$

which assume the following form for a rib on the Fermi surface[1)] ($p_\parallel = 0$, $\epsilon_F = p_c^2/2m_c$), i.e., under the Bragg reflection conditions:

$$\hat{v}_\parallel = 0,$$

$$\hat{v} = \hat{v}_\perp = (1/m_c)[p_c^2 - g^2/4 \mp 2m_c |V_g|]^{1/2}. \qquad (9)$$

Figure 9a shows the section, by the $(1\bar{1}0)$ plane, of a rib of the hole surface of indium drawn in accordance with the 1-OPW model, the rib being formed by the intersection of two Fermi spheres whose centers have the coordinates (1, 1, 1) and (1, 1, −1). The same figure shows the section of a rib, whose shape is given by Eq. (7), in accord-

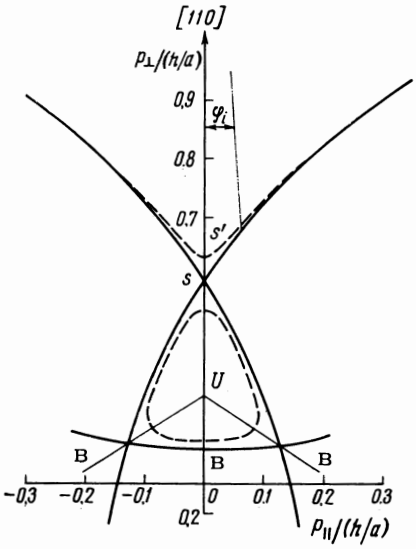

FIG. 9a

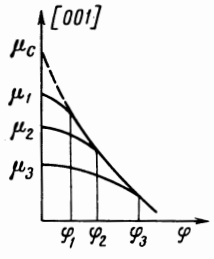

FIG. 9b

FIG. 9a. Sections by the $(1\bar{1}0)$ plane in the 1-OPW model, shown as a continuous curve; sections of the hole surface in the 2-OPW model and of the electron surface in the 3-OPW model (plotted approximately) for the potentials $|V_{111}| = 0.07$ and $V_{002} = -0.055$, shown dashed. B represent the lines of intersection of the Brillouin zone boundaries with the plane of the figure $(1\bar{1}0)$.

FIG. 9b. Qualitative nature of the anisotropy of the effective mass A, calculated from the 2-902 model for various potentials $V_{002}^{(1)} < V_{002}^{(2)} < V_{002}^{(3)}$ for the rotation of the field by an angle φ from the [001] axis.

[1)] Strictly speaking, ϵ_F should be modified to: $\epsilon_F = p_c^2/2m_c + V_0$, in order to make the volume of the new model equal to the volume of the 1-OPW model. However, since usually $V_0 < V_g$ (for example, for aluminum $V_0 \approx 0.2V_{111}$ [11]) and the accuracy of the determination of the lattice potential in the present investigation was not very high (≈20%), we always assumed that $V_0 = 0$.

ance with the 2-OPW model; the lower (minus) sign of the square root in Fig. 7 and g = 2h/c were used. The velocity $\hat{v}$ at the point s′ in Fig. 9a is given by Eq. (9), in which the lower sign in front of $V = V_{002}$ was used. When $V_{002} \to 0$, then $s' \to s$, and the Fermi surface of the 2-OPW model transforms smoothly into the Fermi surface of the 1-OPW model. We can then assume that

$$\hat{v}_c = \lim_{V_{002}\to 0} \hat{v} = (1/m_c)\,[p_c^2 - (h/c)^2]^{1/2} = 0.59\, v_c. \quad (10)$$

This result obtained for the point s in the 1-OPW model (Fig. 9a), is valid for all the ribs in the Fermi surface model and, therefore, we shall now assume that the velocity on the ribs of the 1-OPW model lies in the Brillouin plane and its value is equal to the projection of v_c onto this plane.

It is difficult to calculate the effective mass from the 2-OPW model using formulas (7) and (8) directly, because elliptical integrals are obtained from the integration of Eq. (5). However, it is possible to determine approximately the corrections to the effective mass calculated from the 1-OPW model. Obviously, the main contribution to a change in the integral (5) is made by those segments of the orbit on the Fermi surface, which are near the ribs of this surface. In this case, when the plane of the orbit includes the vector **g** and is therefore orthogonal to the ribs, the effective mass decreases in the segment of the orbit which includes a rib, by an amount

$$\Delta\mu = \frac{[1 + {}^3/_4 \ln (g^2/8m_c|V_g|)]\,(2m_cV_g)^2}{3\pi g\,(1 + g^2/4p_c^2)\,(p_c^2 - g^2/4)^{3/2}}, \quad (11)$$

which is obtained by an approximate integration of (5), using Eqs. (7) and (8). The estimate given in Eq. (11) is valid if $2m_c|V_{\mathbf{g}}| \ll p_c^2 - g^2/4$ and the distance to the nearest rib on the Fermi surface is greater than $2m_cV_{\mathbf{g}}/g$. Thus, the correction $\Delta\mu$ depends quadratically on the value of the potential V_g and is usually small. For example, if we assume that $V_{002} = 0.055(h/a)^2/2m_c$ and $V_{111} = 0.07(h/a)^2/2m_c$, the reduction in the effective mass for the central hole orbit and $\mathbf{H} \parallel [110]$, represents only $\Delta\mu = 0.014$, i.e., 1.9%.

For the orbits whose planes coincide with a Brillouin plane or are close to such a plane, $\Delta\mu$ depends linearly on $V_{\mathbf{g}}$; in such cases, the reduction in the effective mass is due to a reduction in the orbit perimeter. For example, if $V_{002} = 0.055(h/a)^2/2m_c$, the perimeter of the central orbit A on the hole surface for $\mathbf{H} \parallel [001]$ decreases by 3.8% and, consequently, $\Delta\mu/\mu = 6.5\%$. As the plane of an orbit deviates further from a Brillouin plane, the difference between the effective masses obtained from the two models decreases to a minimum. If the magnetic field direction makes, with the [001] axis, an angle larger than

$$\varphi_i \approx \frac{2m_c|V_{002}^{(i)}|2(h/c)}{\sqrt{2}(h/a) - [p_c^2 - (h/c)^2]^{1/2}} \approx 2m_c|V_{002}^{(i)}|/1.5(h/a)_2, \quad (12)$$

then the hole orbit A passes along parts of the surface which are almost undistorted by the presence of a lattice potential (Fig. 9a). Therefore, the nature of the anisotropy of the effective mass A, has qualitatively the form shown in Fig. 9b, for different values of the potential $V_{022}^{(i)}$.

From formulas (1) and (5), it follows that the effective mass is proportional to the period of revolution of a carrier in an orbit. Therefore, if the velocity lies in the plane of an orbit at any point of the orbit ($v_{F\perp} = v_F$) and the orbit period Π is known, then we can determine, directly from the value of the effective mass, the velocity $\tilde{v}_F$ averaged over the orbit:

$$\tilde{v}_F = \Pi / 2\pi\mu. \quad (13)$$

We can also find $\tilde{v}_F$ when, in some parts of the orbit, the direction of v_F makes an angle with the plane of the orbit, the angle being known if the shape of the Fermi surface is known. From the results reported in [3, 6] and in the present paper, it follows that the 1-OPW model is sufficiently good approximation for the hole surface of indium. This model is acceptable because, as shown above, there is only a slight difference between the effective masses calculated using this model and the 2-OPW model, which is closer in shape and dimensions to the real Fermi surface.

We shall carry out calculations for a Fermi surface whose shape and dimensions coincide with the 1-OPW model values, but for which the velocities at various points of the surface are different. The reciprocal of the velocity, averaged out separately for each of the arcs L_n of which the orbit is composed, given by

$$\overline{v_{Fn}^{-1}} = \frac{1}{L_n}\int_{L_n} dl/v_F. \quad (14)$$

A second averaging $\overline{v_{Fn}^{-1}}$ carried out over all the arcs L_n having the angular dimensions φ_n, gives

$$\overline{\overline{v_{Fn}^{-1}}} = \Big(\sum_n \overline{v_{Fn}^{-1}} u_n\varphi_n\Big) \Big/ \sum_n \varphi_n, \quad (15)$$

where $u_n \neq \hat{v}_{cn}/v_c$, if an arc L_n coincides with a rib on the surface or $u_n = 1$ in the remaining cases. Then, using formulas (5) and (6), we can easily show that the measured effective mass μ is related to $\mu_c = m_c/m_e$ by the expression

Table IV

Magnetic field direction	Effective mass* μ	Effective mass* μ_c	$k = \mu/\mu_c$	$\tilde{v}_F \times 10^{-8}$, cm/sec	Type of c.r.
H ‖ [111]	1.60	1.60	1.00	1.09	O_h at limiting point
H ‖ [110]	1.17	1.20	0.98	1.11	A
H ‖ [011]	1.34	1.35	0.99	1.10	A
H ‖ [111]	1.54	1.58	0.97	1.12	A
H ‖ [112]	1.80	~1.86	0.97	1.13	A
∢H, [110] = 20°, (1$\bar{1}$0)	1.43	1.44	0.99	1.10	Q, noncentral
5° ⩽ ∢H, [100] ⩽ 20°, (001)	—	—	1.00	1.09	A
5° ⩽ ∢H, [100] ⩽ 25°, (0$\bar{1}$0)	—	—	1.06	1.03	A
10° ⩽ ∢H, [100] ⩽ 30°, (0$\bar{1}$1)	—	—	0.91	1.20	A
5° ⩽ ∢H, [001] ⩽ 25°, (1$\bar{1}$0)	—	—	0.98	1.11	A
5° ⩽ ∢H, [001] ⩽ 25°, (0$\bar{1}$0)	—	—	1.01	1.08	A
H ‖ [001]	2.17	2.29	0.95	—	β (on electron surface)
H ‖ [110]	0.202	0.203	0.99	—	β (on electron surface)
H ‖ [110]	0.202	0.141 **	1.43	0.76	β (on electron surface)

*Here, μ is the experimental value and μ_c is the 1–OPW model value.
**Determined from the data in[3].

$$\mu = \mu_c v_c \overline{v_F^{-1}} = \mu_c v_c / \tilde{v}_F, \qquad (16)$$

where the notation $\tilde{v}_F = (\overline{v_F^{-1}})^{-1}$ is used. Usually, the difference between the experimental and calculated values of the effective masses is given by the coefficient

$$k = \mu / \mu_c = v_c / \tilde{v}_F, \qquad (17)$$

which is equal to the reciprocal of the orbit-averaged relative Fermi velocity.

Comparison of the results of measurements and calculations for the hole orbits

Table IV gives the values of the effective masses μ_c and μ for the c.r. A and Q, both measured experimentally and calculated from the 1-OPW model, in which it was assumed that $m_c = 1.6m_e$ and $v_c = 1.09 \times 10^8$ cm/sec. Figures 3, 4, 6, and 7 show dashed the μ_c mass anisotropy near the axes [001] and [100]. To make the calculated curve coincide with the experimental data for ∢H, [001] = 10° and ∢H, [100] = 10°, the calculated values were multiplied by a coefficient $k = \mu/\mu_c$, which is also given in Table IV. We can see that all the experimental values agree to within 6% with the values calculated from the 1-OPW model. This agreement can be considered as proving that the mass m_c is within the limits $(1.6 \pm 0.1)m_e$, provided the shapes of the real Fermi surface and of the 1-OPW model are identical. On the other hand, the observed deviations of the measured effective masses from the values calculated using the 1-OPW model, can be explained by means of the 2-OPW model in which it is assumed that $m_c = 1.6m_c$ and an effective lattice potential is determined.

In the present investigation, we were able to measure the effective mass corresponding to the central orbit A, which passed along the ribs of the hole surface of indium for H ‖ [001] (Fig. 10). This orbit is shown dashed in Fig. 7 of [6] and it consists of arcs representing "square caps" and ribs. The velocity along the caps is v_c and approximately isotropic. This follows, for example, from the fact that k = 0.98 for the central hole orbit if H ‖ [110] (Table IV) and that it varies only slightly when the magnetic field is rotated in the (1$\bar{1}$0) plane (Fig. 4). Using Eqs. (15) and (17), we can find the average value of the velocity on a rib of the hole surface (Fig. 9a), which is

$$\overline{(v_F^{-1})^{-1}} = v_c \cdot 0.67 = 0.73 \cdot 10^8 \text{ cm/sec}.$$

This value differs considerably from that expected from the 1-OPW model [Eq. (10)]. This difference can be explained by the 2-OPW model. In fact, if the magnetic field direction approaches the [001] axis, k decreases and, consequently, the difference between the two models increases. This is particularly marked in the angular range ±5° on both sides of the [001] axis in the (0$\bar{1}$0) plane (Fig. 3 and Table III). The Fourier component of the lattice potential is found from the difference $\Delta\mu = \mu_c - \mu$, for H ‖ [001] (Figs. 3 and 9b), using Eqs. (5), (7), and (9):

$$|V_{002}| = (0.055 \pm 0.005)(h/a)^2 / 2m_c$$

and similarly the velocity of holes on a rib is found to be

$$\hat{v}_F = 0.64, \quad v_c = 0.7 \cdot 10^8 \text{ cm/sec}.$$

The agreement between this value of the velocity and that found above indicates that the 2-OPW model describes well the shapes of the ribs on the hole surface of indium and the velocity of carriers on this surface.

Another rough estimate of the potential V_{002} can be obtained from the angle between the direction of the field and the [001] axis at which the difference between the 1-OPW calculated values and the experimental values of the effective mass μ (Figs. 3 and 7) becomes noticeable. From Eq. (12), it follows that

$$|V_{002}| \cong 0.14(h/a)^2/2m_c.$$

The effective mass corresponding to the orbit A for $\mathbf{H} \| [110]$ (Fig. 10) is less than the value calculated from the 1-OPW model by an amount $\Delta\mu = \mu_c - \mu = 0.022$. According to the 2-OPW model and Eq. (11), the reduction in the effective mass is $\Delta\mu_1 = 0.005$ for that part of the orbit which passes along the ribs shown in Fig. 9a. Therefore, the difference $\Delta\mu_2 = \Delta\mu - \Delta\mu_1$ corresponds to that part of the orbit which intersects other ribs, such as a rib R (Fig. 10), formed by the intersection of the Fermi spheres whose centers have the coordinates (0, 0, 2) and (1, 1, 1). The value of this difference determines, according to Eq. (11), the component of the potential

$$|V_{111}| = (0.07 \pm 0.015)(h/a)^2/2m_c.$$

From the difference between the maximum dimension of this orbit (Table III) and the value expected from the 1-OPW model, we can vind V_{111} independently

$$|V_{111}| = (0.04 \pm 0.02)(h/a)^2/2m_c,$$

which is in good agreement with the preceding expression.

The value of k for the orbit A when $\mathbf{H} \| [011]$ indicates that the Fourier component of the potential V_{200} is small and does not affect, within the experimental accuracy the reduction in the effective mass μ (Table IV), i.e.,

$$|V_{200}| \leqslant 0.015(h/a)^2/2m_c.$$

Thus, the estimates of the Fourier components of the lattice potential, given above, allow us to understand why all the values of k given in Table IV for the orbits intersecting the ribs on the hole surface at large angles and passing far from the singularities W and W′ (Fig. 10), are less than unity by 1–3%. The only exception is k = 1.06, but this value is known to be too high because of an error in the crystallographic orientation of the sample InIII. On the other hand, when an orbit approaches the singularities W and W′ on the hole surface, we find that $k \geq 1.0$ (Table IV). It is possible that this departure from the 1-OPW model, not explained by the 2-OPW model, can be accounted for by the 4-OPW model, which gives more accurately the shape of the Fermi surface near the singularities W and W′.

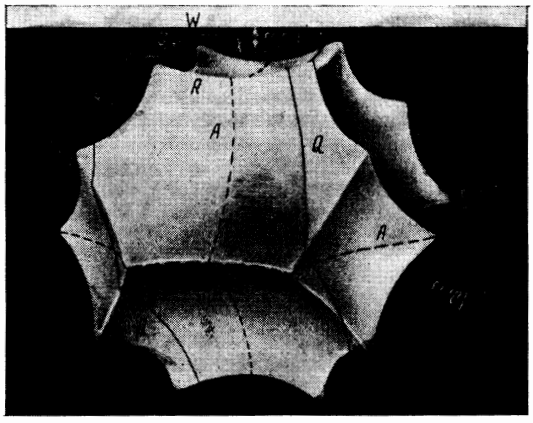

FIG. 10. Hole surface in the second zone, according to the 1-OPW model. U, K, W, and W' represent the symmetry points on the edges of the Brillouin zone according to Bouckaert et al.[19]

ELECTRON FERMI SURFACE OF INDIUM ON THE THIRD ZONE

The anisotropy of the effective electron mass in the crystallographic planes $(0\bar{1}0)$, (001), and $(1\bar{1}1)$ was investigated in [6]. However, the results for the last of these three planes were incomplete, because the experiments were carried out on an imperfect single crystal. Therefore, in the present investigation, we again studied the anisotropy of the effective masses in the $(1\bar{1}1)$ plane using the sample InV of correct crystallographic orientation (Table I). Moreover, we investigated the effective mass anisotropy in the planes $(1\bar{1}0)$ and $(0\bar{1}1)$. All the results are given in Figs. 11 and 12.

Tubes Forming the Electron Surface

The set of effective masses β' and β'' (Figs. 11 and 12 in the present paper, and Fig. 3 in [6]) corresponds to two cylindrical surfaces, which are tubes elongated along the [110] and $[1\bar{1}0]$ axes. This follows from the plots of the effective masses β' and β'' which are practically straight lines in their middle parts [Eq. (6) in [15]], with minimum values for $\mathbf{H} \| [100]$. On the other hand, the β tubes have constrictions because the plots of the effective masses β differ considerably from straight lines when the field $\mathbf{H}$ is rotated away from the projec-

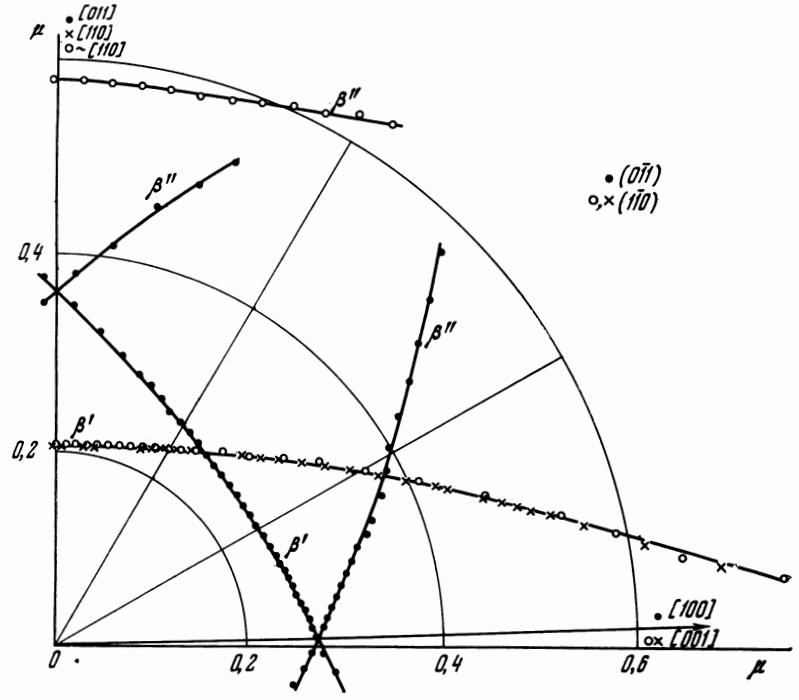

FIG. 11. Anisotropy of the effective electron mass in indium. Symbols represent the masses measured by rotation of the field in two planes: × and ○ – (1$\bar{1}$0) (samples InII and InIV, respectively); ●–(0$\bar{1}$1) (sample InVI). The directions of the axes, corresponding to these planes, and the planes themselves are shown in the figure by the same symbols.

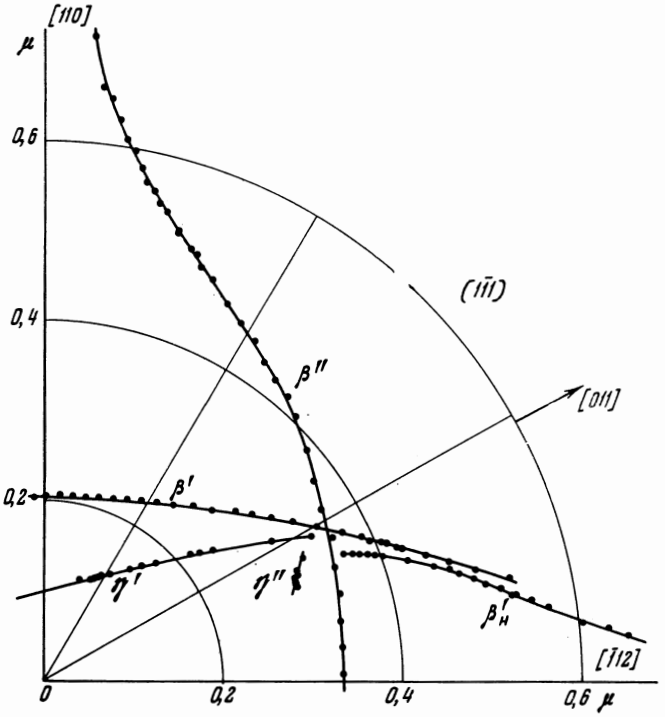

FIG. 12. Anisotropy of the effective electron mass in indium in the (1$\bar{1}$1) plane. Sample InV.

tion of the [110] axis onto the plane of the sample.

In indium, whose tetragonal lattice has three symmetry planes (1$\bar{1}$0), (110), and (001), as well as a fourfold axis [001], the Fermi surface can have only four types of tube, which cannot be made congruent by translation but are elongated along the [110] and [1$\bar{1}$0] axes if they are intersected by the symmetry planes. In this case, a rotation by 180° about the [001] axis and a reflection in the (001) plane make congruent the orbits on a pair of tubes having parallel axes. Therefore, only two c.r. can be observed for two pairs of such tubes. This is confirmed by experiment.

The foregoing conclusions about the shape of the tubes and their positions in the momentum space are in agreement with the 1-OPW model (Fig. 13), which consists of tubes β which become narrower at their ends and are elongated along [110] type axes and intersected by the symmetry planes (001), (1$\bar{1}$0), and (110). At the points W in

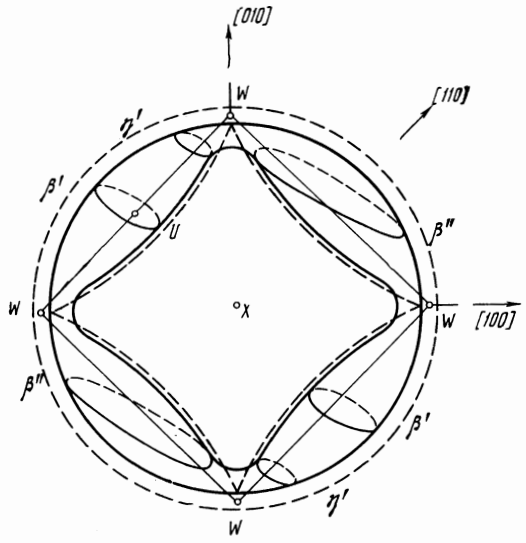

FIG. 13. Electron Fermi surface of indium in the third zone, plotted from the results of the present investigation and the paper[3]. The dashed curves represent the 1-OPW model. The β', β'', and η orbits are shown. U, X, and W represent the symmetry points (Fig. 10).

the 1-OPW model, the tubes join thinner tubes α, elongated along axes of the [011] type (Fig. 4a in [6]). However, the present and previous[3,6] investigations have not yielded any data supporting the existence of the α tubes. In the absence of a symmetry plane of the $(0\bar{1}1)$ type, the indium lattice need not have a cross section for $\mathbf{H} \parallel [011]$ which would be extremal in respect of the effective mass. It is possible that this is why the c.r. of the α tubes was not observed but quantum oscillations of the cross sections of the α tubes were reported in [2].

From the c.r. and size effect[3] investigations, it follows that the electron Fermi surface of indium in the third zone is topologically similar to a torus and consists of four β tubes joined end to end. The principal dimensions of such a surface were reported in [3]; the value of the perimeter of the central orbit for $\mathbf{H} \parallel [110]$ makes it possible to determine the average electron velocity by means of formula (13). This velocity is found to be $\tilde{v}_F = 0.76 \times 10^8$ cm/sec (Table IV), i.e., it is almost equal to the velocity of holes along a rib on the hole surface. This result is in agreement with the observation that the carrier velocities near the boundary of a Brillouin zone should be less than they are away from this boundary.

Noncentral electron orbits

In [6], we drew your attention to the profile of the c.r. line β (Fig. 2 in [6]), which could have been due to the superposition of two c.r. corresponding to similar effective masses. In the $(1\bar{1}1)$ plane (Fig. 12) for $\measuredangle \mathbf{H}, [110] = 70-80°$, the c.r. resolution was sufficiently good to investigate the dependence of the c.r. line on the inclination of the magnetic field to the surface of a sample (Fig. 14). It was found that the β'_n c.r., corresponding to a lighter mass, depended strongly on the inclination of the field and was therefore associated with a noncentral orbit. As the field was rotated away from the [110] axis, the β'_n c.r. became gradually stronger, while the β' c.r. weakened (Fig. 11). Obviously, this took place not only in the $(1\bar{1}1)$ plane but also in other planes. However, due to the insufficient resolution of the c.r. ($\delta H^{-1}/H^{-1} = 1/20$), only an irregularity was observed in the dependence of the c.r. position on the magnetic field direction [cf., for example, Fig. 3 in [6] or the graph of β'' for the $(0\bar{1}1)$ plane when $\measuredangle \mathbf{H}, [100] = 20-30°$ in Fig. 10]. The existence of a noncentral c.r. β'_n corresponding to a smaller effective mass, provides additional evidence of the narrowing of the β tubes at their ends.

Neck of tubes

In the $(1\bar{1}1)$ plane, we observed first- and second-order c.r. of considerable amplitude, corresponding to the smallest effective mass η observed in indium (Fig. 12). Its value was 0.11 for $\measuredangle \mathbf{H}, [110] = 20°$. The anisotropy of this effective mass indicates that indium has a tubular Fermi surface with an axis whose projection onto $(1\bar{1}1)$ plane makes an angle of $16° \pm 1°$ with the direction [110]. Bearing in mind the electron surface model described above, we may conclude that the effective mass η is associated with an orbit on a narrow constriction at the end of a β' tube close to the place where it joins another tube β'' (Fig. 13). The axis of this constriction (neck) makes a fairly large angle with the tube axis, which is parallel to [110]. For example, in aluminum, whose electron surface is also in the form of "square torus,"[18,20] the axes of the necks make an angle of 20–25°

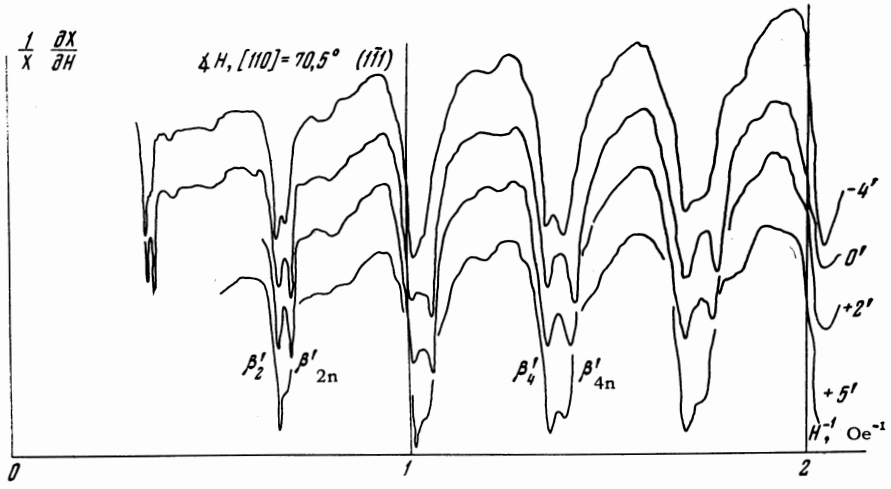

FIG. 14. Recordings of the c.r. spectra β' and β'_n for the β tubes of the electron surface for various angles of inclination of the field to the sample surface. The orientations of the surface and the field are given above the curves; the angles of inclination are to the right of the curves.

with the direction [110] (the value of this angle was estimated from the anisotropy of the α-oscillations shown in Fig. 5c of [20]). In indium, this angle, which lies in the (001) plane, can be easily determined from its projection onto the (1$\bar{1}$1) plane: the required angle is equal to $\tan^{-1}(\cos 58.5° \cdot \cot 16°) = 29° \pm 1°$. This value is in good agreement with the shape of the electron surface (Fig. 13).

The neck size can be estimated from the value of the angle between the axis of a β tube and the direction of the field **H** at which the β orbit enters the neck and becomes discontinuous. It is evident from Figs. 11 and 12 in the present communication and from Fig. 3 in [6] that, for various crystallographic planes, this angle lies within the range $6° \pm 2°$. Since the length of an edge of the Brillouin zone is 0.8(h/a), the perimeter of the neck is

$$\Pi_\eta = 0.8\pi \tan(6° \pm 2°)(h/a) = (0.25 \pm 0.08)(h/a).$$

Assuming that the electron velocity on the neck lies in the plane of the orbit, we can use formula (13) to estimate the electron velocity $\tilde{v}_{F\eta}$ on the neck of a tube:

$$\tilde{v}_{F\eta} / \tilde{v}_{F\beta} = (\Pi_\eta / \Pi_\beta)\mu_\beta / \mu_\eta = 0.9 \pm 0.2; \qquad (18)$$

here, $\Pi_\beta = 0.61(h/a)$, according to [3]. This rough estimate shows that the velocity on the neck is approximately the same as in the middle part of the tube.

CONCLUSIONS

The models of the Fermi surfaces of indium, aluminum, and lead, considered in the almost-free electron approximation, have much in common.[6] The similarity of the Fermi surfaces of these metals was confirmed by the present investigation, since many effective masses detected in indium were found to be analogs of the corresponding masses in aluminum[13, 16] and in lead,[15] both in respect of their anisotropy and the ratios of their values.

The velocities of holes and electrons (Table IV) were found by comparing the measured values of the effective masses with the values calculated from the 1-OPW model of indium. In particular, the velocity of holes on a rib of the Fermi surface was found to be 0.73×10^8 cm/sec; the velocities of holes on remaining parts of the hole surface were considerably greater, for example, $v_F = 1.09 \times 10^8$ cm/sec for $\mathbf{H} \| [111]$.

From the results of the present investigation, we may conclude that, with some exceptions, the anisotropy of the effective masses and of the velocities of carriers in indium is explained satisfactorily by the 1-OPW model, in which the carrier mass is taken to be $1.6m_e$. The exceptions, which cannot be explained by the 1-OPW model, are the following experimental observations:

a) the deviation of the anisotropy of the effective mass A from the calculated value near the [100] (Fig. 6) and [001] (Fig. 3) axes;

b) the small reduction in all the extremal dimensions of the Fermi surface and of the effective masses compared with the values found from the model (Fig. 7, Tables III and IV);

c) the absence of the cyclotron resonance for the tubes of the electron surface;

d) a smaller electron velocity (by a factor of ~1.4), compared with the hole velocity (Table IV);

e) the Fermi surface area S being ~0.8 of the model surface S_c. This reduction factor was found as follows. The coefficient γ of the linear term in the electronic specific heat is, as is known,[21] proportional to the integral $\int ds/v_F$, taken over the whole Fermi surface S, and consequently

$$\int_S dS/v_F = S/\tilde{v}_F,$$

where $\tilde{v}_F \sim v_c/1.6$, according to our investigation. On the other hand, γ for indium[7,21] is 1.3 times less than the value calculated from the 1-OPW model. Consequently, $S/S_c = 0.8$.

All these differences, found by comparing the experimental data with the 1-OPW model, can be eliminated by replacing it with another model, developed in the approximation of several OPW, for example, 2-OPW [differences a), b), and e)] or 3-OPW [differences c) and d)].

The validity of this conclusion in respect of differences a) and b) has been proved here earlier. A comparison with the 2-OPW model gave the following Fourier components of the effective lattice potential:

$$|V_{111}| = 0.07 \pm 0.015, \qquad |V_{002}| = 0.055 \pm 0.01,$$

$$|V_{200}| < 0.015$$

[the values of the potential are given here, and later, in units of $(h/a)^2/2m_c = 0.329$ Ry, $\epsilon_F = p_c^2/2m_c = 1.21$].

Remarks on difference e)

These components of the potential can be used to estimate approximately, within the limits of the accuracy of the 2-OPW model, the total area of the Fermi surface of indium $S = 0.85S_c$. This reduction in the Fermi surface area in the 2-OPW model takes place in a strip near the ribs and, in the first approximation with respect to $V_{\mathbf{g}}$, it is given by

$$\Delta S_g = 4\pi |2m_c V_g| [(p_c^2 - g^2/4)^{1/2} - p_c] / g.$$

A similar result, $S = 0.93S_c$, follows from the measurements of the anomalous skin effect.[22] The values obtained are in agreement with the experiments on the cyclotron resonance and on the specific heat.

The shape of the electron Fermi surface of indium, and the electron velocities far from the singularities W and W', should be compared with the 3-OPW model.[23] However, because complete calculations based on this model were not carried out in [23], the comparison given below will be made only in respect of certain details.

Remarks on difference c)

The problem of the existence of the α tubes in the electron surface of indium may be considered on the basis of the 3-OPW model. The difference between the Fermi and electron energies at a point K in the 1-OPW model (Fig. 10) amounts to 0.11. The increase in the energy of the bottom of the band lying close to the point K is, according to the 3-OPW model, approximately equal to $|V_{200} + \sqrt{2}\,|V_{111}|| = 0.10 \pm 0.03$ if the components of the potential given above are substituted. This means that the α tubes in the 3-OPW model are either very small or do not exist at all.

Remarks on difference d)

The values of the effective mass β', corresponding to the central orbit on the electron surface for $\mathbf{H} \parallel [110]$, are practically identical for the 1-OPW and 3-OPW models [the difference is $\sim 1\%$, according to Eq. (11)], and agree with experiment: $\mu = 0.202 = 0.99\mu_c$. On the other hand, the smaller orbit perimeter,[3] compared with the 1-OPW model, causes a reduction in the electron velocity [Eq. (13)]. Consequently, to check whether the 3-OPW model explains correctly why the electron velocities are lower than the hole velocities, we must find whether a calculation based on the 3-OPW model gives an orbit perimeter agreeing with the experiments of Gantmakher and Krylov.[3] We shall only calculate one dimension of a β tube in the $(1\bar{1}0)$ plane along the [110] direction (Fig. 9a) using the 3-OPW model.[23] The calculation gives $0.22(h/a)$ for $V_{002} < 0$ or $0.19(h/a)$ for $V_{002} > 0$. The first of these values is identical with the result reported in [3]: $(0.22 \pm 0.01)(h/a)$. Thus, from this agreement of the calculation with experiment, we can additionally conclude that $V_{002} < 0$.

The values of the components of the effective potential, determined in the present investigation, are in satisfactory agreement with the theory of the effective potential[24] which has only one parameter β; this parameter can be found experimentally. The best agreement between the experimental data and Harrison's theory[24] is obtained for $\beta = 34 \pm 2$. In this case the calculation gives

$$V_{111} = -0.10 \pm 0.01, \; V_{002} = -0.05 \pm 0.01,$$

$$V_{200} = 0.003 \pm 0.012.$$

From the experiments on the electrical resistance of alloys of indium with other metals, it follows that $\beta = 31 \pm 5$.[25] Bearing in mind the possible error in the determination of β, the agreement between these values can be regarded as satisfactory. Recent calculations[26] of the effective potential are in poorer agreement with experiment: an approximation using Eq. (4) in [24] gives $\beta = 42$.

The electrical resistance of liquid indium gives gives[27] the value $|V_{\mathbf{g}}| = 0.085$, averaged out over a certain range near $g = 2p_c$. This value is also in satisfactory agreement with the experi-

mentally determined components of the lattice potential.

In conclusion, we note that in the present investigation the potentialities of the cyclotron resonance method of experimental investigation of the properties of carriers in a metal were used to measure the Fermi velocities and their anisotropy and to determine the components of the effective potential of the crystal lattice of the metal.

The authors are grateful to P. L. Kapitza for his constant interest in this investigation, to G. V. Gantmakher, I. P. Krylov, and V. S. Édel'man for discussing the results, and to G. S. Chernyshev and V. A. Yudin for their technical assistance.

[1] J. A. Rayne, Phys. Rev. **129**, 652 (1962).

[2] G. B. Brandt and J. A. Rayne, Phys. Rev. **132**, 1512 (1963); Phys. Letters **12**, 87 (1964).

[3] V. F. Gantmakher and I. T. Krylov, JETP **47**, 2111 (1964), Soviet Phys. JETP **20**, 1418 (1965); JETP **49**, 1054 (1965), Soviet Phys. JETP **22**, 734 (1966).

[4] Yu. P. Gaĭdukov, JETP **49**, 1049 (1965), Soviet Phys. JETP **22**, 730 (1966).

[5] J. G. Castle, Jr., B. S. Chandrasekhar, and J. A. Rayne, Phys. Rev. Letters **6**, 409 (1961).

[6] R. T. Mina and M. S. Khaĭkin, JETP **48**, 111 (1965), Soviet Phys. JETP **21**, 83 (1965).

[7] H. R. O'Neal and N. E. Phillips, Phys. Rev. **137**, A748 (1965).

[8] R. T. Mina and M. S. Khaĭkin, JETP Pis'ma **1**, No. 2, 34 (1965), JETP Letters **1**, 60 (1965).

[9] W. J. Tomasch, Phys. Rev. Letters **16**, 16 (1966); W. L. McMillan and P. W. Anderson, Phys. Rev. Letters **16**, 85 (1966); W. J. Tomasch and P. Wolfram, Phys. Rev. Letters **16**, 352 (1966).

[10] W. A. Harrison, Phys. Rev. **118**, 1190 (1960).

[11] M. S. Khaĭkin, PTÉ No. 3, 95 (1961).

[12] M. S. Khaĭkin and V. S. Édel'man, JETP **47**, 878 (1964), Soviet Phys. JETP **20**, 587 (1965).

[13] V. P. Naberezhnyĭ and V. P. Tolstoluzhskiĭ, JETP **46**, 18 (1964), Soviet Phys. JETP **19**, 13 (1964).

[14] É. A. Kaner and M. Ya. Azbel', JETP **33**, 1461 (1957), Soviet Phys. JETP **6**, 1126 (1958).

[15] R. T. Mina and M. S. Khaĭkin, JETP **45**, 1304 (1963), Soviet Phys. JETP **18**, 896 (1964).

[16] F. W. Spong and A. F. Kip, Phys. Rev. **137**, A431 (1965).

[17] H. A. Bethe and A. Sommerfeld, Electron Theory of Metals (Russ. Transl., ONTI, 1938).

[18] N. W. Ashcroft, Phil. Mag. **8**, 2055 (1963).

[19] L. P. Bouckaert, R. Smoluchowski, and E. Wigner, Phys. Rev. **50**, 58 (1936).

[20] E. P. Vol'skiĭ, JETP **46**, 123 (1964), Soviet Phys. JETP **19**, 89 (1964).

[21] C. Kittel, Introduction to Solid State Physics (2nd edition), Wiley, New York, 1956 (Russ. Transl., Fizmatgiz, Moscow, 1963).

[22] P. N. Dheer, Proc. Roy. Soc. (London) **A260**, 333 (1961).

[23] W. A. Harrison, Phys. Rev. **118**, 1182 (1960).

[24] W. A. Harrison, Phys. Rev. **131**, 2433 (1963).

[25] W. A. Harrison, Rev. Mod. Phys. **36**, 256 (1964).

[26] A. O. E. Animalu and V. Heine, Phil. Mag. **12**, 1249 (1965).

[27] C. C. Bradley, T. E. Faber, E. G. Wilson, and J. M. Ziman, Phil. Mag. **7**, 865 (1962).

Translated by A. Tybulewicz
10